ACS APPLIED MATERIALS & INTERFACES

Research Article

www.acsami.org

Delithation, Exfoliation, and Transformation of Rock-Salt-Structured Li_2TiO_3 to Highly Exposed {010}-Faceted Anatase

Yi-en Du,[†,‡] Dejian Du,[†] Qi Feng,*[,‡] and Xiaojing Yang*[,†]

[†]Beijing Key Laboratory of Energy Conversion and Storage Materials, College of Chemistry, Beijing Normal University, Beijing, 100875, China

[‡]Department of Advanced Materials Science, Faculty of Engineering, Kagawa University, 2217-20 Hayashi-cho, Takamatsu-shi, 761-0396, Japan

Supporting Information

ABSTRACT: {010}-Facet-exposed anatase TiO_2 crystals exhibit the highest photoreactivity among the exposed facets. To obtain a higher exposure rate of this facet, the work investigated the transformation of the nanosheets with cavities within the layers derived from a rock-salt-structured Li_2TiO_3 precursor. All the lithium ions were extracted from the precursor by H^+/Li^+ ion exchange in HCl aqueous solutions, and after tetramethylammonium ions were intercalated, the precursor can delaminated into the nanosheets. The $[TiO_3]^{2-}$ nanosheets were hydrothermally treated under different temperatures and pH values. The results showed that the anatase phase was formed in a wider range of pH and temperature, compared with using nanoribbons of $[Ti_4O_9]^{2-}$ and nanosheets of $[Ti_{1.73}O_4]^{1.07-}$. At low pH, [111]-faceted nanorod-shaped anatase nanocrystals were formed preferentially, and the nanocrystals preferentially grow along the [001] direction with the increase of solution pH, leading to a large percentage of {010} facets on their surface. The photocatalytic activity increases with the increase of exposure rate of {010} facets.

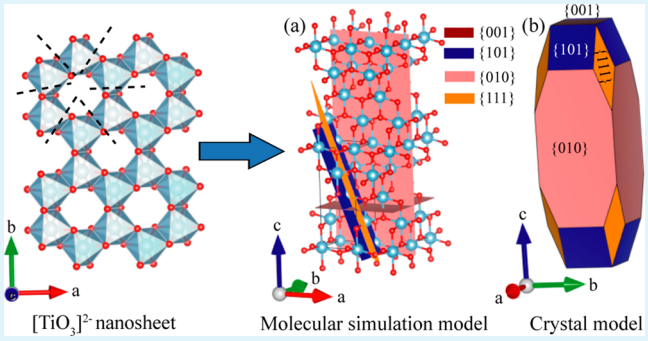

KEYWORDS: *anatase TiO_2, [111] facets, {010} facets, exposure rate, photocatalysis*

1. INTRODUCTION

Shape-controlled synthesis of inorganic nanocrystals with exposed high-energy or reactive facets has attracted intensive interest over the past decade, due to their fascinating shape-dependent properties,[1−3] as well as their great importance in fundamental studies and technological applications.[4−6] Such efforts were made in the past few years to design and synthesize anatase-type TiO_2 nanocrystals with different morphologies and exposed specific facets,[7−17] because anatase phase (tetragonal, space group $I4_1/amd$) usually exhibits superior photocatalytic properties for degradation of organic molecules and excellent photovoltaic performances among the four crystallographic TiO_2 phases,[18−20] others of which are rutile (tetragonal, $I4_1/amd$), brookite (orthorhombic, $Pbca$), and TiO_2(B) (monoclinic, $C2/m$). For the exposed facets of anatase TiO_2, {001}, {100}/{010}, and {101} facets are usually reported. Two factors are considerable in the determination of the photoreactivity: (1) the suface energy[21] and (2) the surface electronic structure (the power of photoexcited charge carries) and surface atomic structure (the density of under-coordinated titanium atoms).[22] The surface energy increases in the order of {101} facet (0.44 J/m^2) < {100}/{010} facet (0.53 J/m^2) < {001} facet (0.90 J/m^2).[21] The superior electronic and surface atomic structures of the {010} facet account for its highest photoreactivity, though its surface energy is not the highest.[22]

Crystal facets of rutile ({011} and {110}) and anatase ({001} and {011}) TiO_2 particles and their roles in photocatalytic reactions were first reported by Ohno et al.[23] After that, Wen et al.[24] first obtained exposed {010} facets using a soft chemical process by utilized $[Ti_{1.73}O_4]^{1.07-}$ nanosheets as the precursor. Microsized anatase TiO_2 crystals with 47% exposed {001} facets was synthesized by using TiF_4 as the raw material and hydrofluoric acid as a morphology-controlling agent under hydrothermal conditions by Yang et al.,[7] and 89% exposed {001} facets obtained by a similar strategy exhibited higher photocatalytic efficiency than commercial Degussa P25 sample.[25] After that, truncated rhombic anatase TiO_2 nanocrystals with exposed {001} facets using titanium *n*-butoxide as the precursor and oleic acid, oleylamine, and ethanol as the capping agents were synthesized.[26] Han et al. also have synthesized truncated bipyramidal anatase TiO_2 nanoparticles with square or rectangular bases by using K-titanate nanowires as the precursor and urea or ammonium carbonate as the capping agents.[27] In general, the syntheses of anatase crystals

Received: January 9, 2015
Accepted: March 30, 2015
Published: March 30, 2015

DOI: 10.1021/acsami.5b00227
ACS Appl. Mater. Interfaces 2015, 7, 7995−8004

with exposed {001} facets and various morphologies, such as sheet,[8] rhombic-shaped,[26] truncated bipyramid,[27] hollow box,[28] sphere,[29] and cuboid,[30] were extensively studied. Hydrofluoric acid[7] or other fluorine-containing species were usually employed as capping agents, such as titanium fluoride,[8] ammonium fluoride,[31] sodium fluoride,[32] ammonium hexafluorotitanate,[33] and sodium fluoroborate.[34] Recently, fluorine-free capping agents, such as ethylene glycol,[35] 2-propanol,[8] oleic acid,[26] urea,[27] and carboxylic acid,[28] were developed.

However, relatively fewer studies were reported on the synthesis of anatase nanocrystals with dominant {010} facets.[20,36,37] Employing both oleic acid and oleylamine as capping agents in the presence of water vapor, rhombic, truncated rhombic, dog-bone-like, truncated and elongated rhombic, and bar-like anatase nanocrystals with exposed {010} facets were synthesized by a solvothermal route.[26] Anatase TiO_2 rods with dominant reactive {010} factes were synthesized by hydrothermally treating lepidocrocite-type $Cs_{0.68}Ti_{1.83}O_4/H_{0.68}Ti_{1.83}O_4$ particles.[11] Recently, using HF as the morphology-controlling agent/shape-directing agent, elongated truncated tetragonal bipyramid anatase particles with a large percentage of exposed {010} facets were obtained by hydrothermal treatment of the titanium oxysulfate solution, which exhibited a higher photoreactivity than {101} and {001} facets.[22]

Besides being unexpectedly toxic and corrosive,[27] the fluoride ions in fluorine-containing compounds that are added to passivate the crystal planes are difficult to remove from the crystal surface.[20] The organic molecules, such as oleic acid or oleylamine, may reduce the percentages of high-energy facets and impose environmental contamination because of the evaporation of organic molecules.[38] And the alkoxide precursors, such as isopropoxide, may increase the difficulty of achieving high-quality and uniform anatase TiO_2.[39] Feng et al. developed an alternative route to prepare anatase TiO_2 nanocrystals with exoposed {010} facets via a topotactic transformation reaction by hydrothermal treatment of the $[Ti_{1.73}O_4]^{1.07-}$ nanosheets in the absence of any morphology-controlling agents.[40] Using this method, most recently, we reported the transformation of $[Ti_4O_9]^{2-}$ nanoribbons as precursor to anatase nanocrystals with [111]-facet (the facet vertical to the [111] direction) and {010}-facet exposure.[41] In the current work, the transformation of the metatitanic $[TiO_3]^{2-}$ nanosheets, which contain cavities within the layers, into anatase was investigated in order to develop this method and to obtain a high exposure rate of the {010} facet.

For the metatitanic salt of Li_2TiO_3, one-third of the Li^+ ions exist in the layer of the TiO_6 octahedron formed framework; thus, to obtain the nanosheets, delithation should be studied, followed by the intercalation of tetramethylammonium (TMA^+) ions and exfoliation. The possible reaction mechanism of the crystal transformation was compared with that of other precursors, and photocatalytic activities of the obtained anatase nanocrystals are investigated herein.

2. EXPERIMENTAL SECTION

2.1. Preparation of Metatitanic Nanosheets from H_2TiO_3. Titanium dioxide (TiO_2, 98.5%) and lithium carbonate (Li_2CO_3, 99.0%) were purchased from Wako Pure Chemical Industries, Ltd. From the reagents, layered lithium titanate Li_2TiO_3 (LTO) was synthesized via conventional solid-state calcination.[42] Briefly, the reagents with a stoichiometric ratio were ground by ball-milling using 5 mm diameter alumina balls for 6 h at a rotational speed of 50 rpm, and the obtained powder was heated in a muffle furnace at 850 °C for 24 h using an alumina crucible. The obtained LTO (10.0 g) was immersed in a 1.0 mol/L HCl aqueous solution (1 L) and stirred at room temperature for 3 days, while the HCl solution was replaced daily with a fresh one,[43] to prepare $H_2TiO_3{\cdot}nH_2O$ (HTO).

The HTO (4.0 g) and 12.5% tetramethylammonium hydroxide (TMAOH) (Wako Pure Chemical Industries, Ltd.) solution (40 mL) were sealed in a Teflon-lined stainless steel autoclave with a capacity of 70 mL and maintained at 100 °C for 24 h under stirring conditions to prepare TMA^+-intercalated layered metatitanic compound, after which the autoclave was allowed to cool to room temperature. The resulting white sample was dispersed in 360 mL of Milli-Q water at room temperature for 3 days with stirring. A stable metatitanic nanosheet colloidal suspension was obtained.

2.2. Synthesis of TiO_2 Nanocrystals. The nanosheet colloidal suspension was adjusted to the desired pH value with a 3 mol/L HCl solution and 1 mol/L TMAOH solution, and subsequently, the suspension (40 mL) was hydrothermally treated using the same autoclave described above at the desired temperatures for 24 h. After the autoclave was cooled to room temperature, the product was separated from the solution by centrifugation, washed several times with Milli-Q water, and dried using a freeze-drier. The sample obtained is designated as T*x*-pH*y*, where *x* and *y* refer to the treatment temperature and pH value of the colloidal suspension, respectively. Note that we tried to synthesize TiO_2 nanoparticles directly from HTO without the treatment in TMAOH, but the result showed that the morphology of the obtained anatase particles was similar to that of HTO.

2.3. Characterization. The X-ray diffraction (XRD) pattern was collected in a powder X-ray diffractometer (Shimadzu XRD-6100 diffractometer with Cu Kα radiation, λ = 0.154 06 nm, operated at 40 kV and 30 mA). The electron microscope observation was carried out using field emission scanning electron microscopy (FE-SEM) (Hitachi S-90X, operated at 15 kV and 10 μA) and transmission electron microscopy (TEM) (JEOL JEM-3010, operated at 200 kV) with selected-area electron diffraction (SAED). The thermogravimetry and differential thermal analysis (TG–DTA) was carried out on a Shimadzu DTG-60H at a heating rate of 10 °C/min. The Brunauer–Emmett–Teller (BET) surface areas of the samples were determined by a Quantachrome Quadra Win Instruments using nitrogen gas adsorption at −196 °C, and the sample was degassed before the adsorption for 3 h at 120 °C.

The contents of lithium and titanium in LTO and HTO were analyzed using inductivity coupled plasma emission spectrometry (ICP-ES, JARREL-ASH ICPA-9000). For this analysis, the solid samples were dissolved through the following steps: (1) the sample (100 mg) was placed into a Teflon-lined stainless steel autoclave with a capacity of 50 mL, and then hydrofluoric acid (2 mL) and perchloric acid (2 mL) were added into the autoclave; (2) the autoclave was slightly heated to evaporate the hydrofluoric acid until no white fog appeared; (3) after cooling to room temperature, the solution was transferred to a 500 mL volumetric flask and diluted with Milli-Q water to volume to be ready for further diluting for the ICP measurement. The compositions of the samples were calculated according to the analyzed contents of lithium and titanium.

2.4. Photocatalytic Activity. The photocatalytic activity of the TiO_2 nanocrystals was evaluated by the photodegradation of methylene blue (MB, obtained from Waldeck GmbH & Co KG) in a 200 mL quartz beaker under ambient temperature. A 250 W ultraviolet lamp was used as a light source, and the distance between the lamp and the sample was 80 cm. An aqueous suspension of MB (150 mL, 1.56×10^{-5} mol L^{-1}) and 30 mg of the TiO_2 nanocrystals sample were placed in the beaker. Prior to photoreaction, the colloidal suspension was magnetically stirred for about 2 h in darkness to establish the adsorption–desorption equilibrium. At intervals of 10 min, 3 mL of solution was drawn from the suspension and immediately centrifuged to remove the TiO_2 nanocrystals. The concentration of MB aqueous solution was determined by measuring the absorbance using a TU-1901 spectrophotometer (Beijing Purkinje General Instrument Co. Ltd.). The photocatalytic degradation kinetic

DOI: 10.1021/acsami.5b00227
ACS Appl. Mater. Interfaces 2015, 7, 7995–8004

was studied, and the linear simulation of degradation of the MB solution can be accounted for by a pseudo-first-order model, called the Langmuir–Hinshelwood (L-H) model,[44] calculated as $\ln(C_0/C_t) = k_{app}t$, where C_0 and C_t represent the initial equilibrium concentration and the concentration at a certain irradiation time of the MB solution, respectively; k_{app} and t represent the apparent reaction rate constant and the reaction time, respectively. The photodegradation percentage was calculated[45] according to the equation $\eta = (C_0 - C_t)/C_0 \times 100\%$. For comparison, Degussa P25 (obtained from Nippon Aerosil Ltd.), the nanocrystalline TiO_2 powder (~80% anatase and ~20% rutile), was also measured.

3. RESULTS AND DISCUSSION

3.1. Nanosheet with Pores in the Intralayer. Figure 1A shows that the LTO sample was well-crystallized and that the

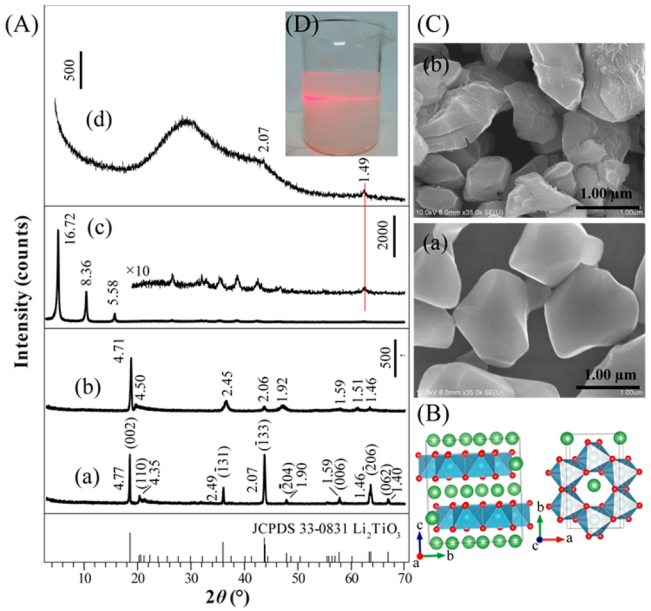

Figure 1. (A) XRD patterns for (a) LTO, (b) HTO, (c) TMA^+-intercalated, and (d) exfoliated metatitanic acid samples. (B) Structural model of LTO viewed along the [100] and [001] directions, respectively. (C) SEM images of (a) LTO and (b) HTO. (D) Tyndall light scattering of the colloidal suspension. *d*-values are in angstroms.

analyzed composition $Li_{2.06}TiO_3$ is close to the stoichiometric Li_2TiO_3. The crystal has the rock-salt structure with monoclinic symmetry, space group *C*2/*c* (JCPDS No. 33-0831). The lattice parameters are calculated according to the pattern of Figure 1A(a) as $a = 0.5067(5)$ nm, $b = 0.8765(6)$ nm, $c = 0.9713(7)$ nm, $\beta = 100.10(6)°$. As shown in Figure 1B, each central TiO_6 octahedron connects with the three adjacent TiO_6 octahedrons by sharing three meta-position edges of the octahedron, and six TiO_6 octahedrons form a hexagonal cavity, forming the $[TiO_3]^{2-}$ layers. Li^+ ions in the crystal have three sites, 4e, 4d, and 8f (Wyckoff index); those at 4e are in the hexagonal cavity and others are in the interlayer. That is, two kinds of Li^+ can be represented by $Li_{1.5}[Li_{0.5}TiO_3]$, which shows Li^+ ions in the cavity (0.5) and interlayer (1.5). After treatment in the HCl aqueous solution, almost all the Li^+ ions were extracted by the H^+/Li^+ ion exchange (Table 1). The chemical analysis result also reveals that H_2O does not intercalate into the interlayer. This coincides with the decrease of the basal spacing from 4.77 Å of LTO to 4.71 Å of HTO [Figure 1A(b)]. The SEM images (Figure 1C) show that the particle retained the shape but some

Table 1. Chemical Analysis Results

	content found (calcd)/wt %		
sample	Li	Ti	formula
LTO	12.9 (13.1)	42.8 (43.4)	$Li_{2.064}TiO_3$
HTO	0.0499 (0.0488)	50.1 (48.9)	$H_{1.993}Li_{0.007}TiO_3$

of the smooth surface became coarse, implying that the protonation process hardly breaks the particle even though the Li^+ ions in the intralayer were extracted, unlike for the extraction of all Li^+ ions from Li_2MnO_3.[46]

The basal spacing was enlarged to 16.72 Å [Figure 1A(c)] after hydrothermal treatment in the TMAOH solution, indicating that TMA^+ ions were successfully intercalated into the interlayer space by the TMA^+/H^+ ion exchange. Because the thickness[47] of a Na-birnessite (layered manganese oxide) layer is 4.5 Å and the atomic radius of titanium (1.47 Å) is a little bigger than that of manganese (1.37 Å), the thickness of a metatitanic nanosheet is evaluated as 4.6 Å. In view of the height of TMA^+ being 5.3 Å[48] and the diameter of a water molecule being 2.8 Å,[47] the large basal spacing implies that the TMA^+-intercalated sample in its wet state contains approximately double layers of water and a monolayer of TMA^+ [4.6 + 5.3 + (2 × 2.8) = 15.5 Å] in the interlayer. This arrangement can be explained by comparing the area per unit charge (S_{charge}). S_{charge} of the nanosheet is 0.028 nm^2 [$a \times b/(4 \times$ charge per TiO_6 octahedron)/2, where the lattice parameters a and b are considered the same as those of LTO and the charge per TiO_6 octahedron is −2] assuming the cavity is without a proton or 0.037 nm^2 if considering the cavity occupied by a proton (charge per TiO_6 octahedron is 1.5). In both cases, the S_{charge} value of the layer is much less than that of TMA^+ (0.22 nm^2),[41,48] so the complete ion exchange of H^+ with TMA^+ would be difficult; namely, partial TMA^+/H^+ ion exchange occurs in the intercalation reaction, due to the large size of the TMA^+ ion. The H^+ ions in the interlayer would be more easily exchanged by TMA^+ ions than those in the cavity.

The XRD pattern of the dispersed sample [Figure 1A(d)] shows a halo with a small peak at $d = 1.49$ Å. The peak was observed in the pattern of the TMA^+-intercalated sample, and we consider that it is very possibly the refection of the plane in the intralayer, even though it is difficult to index the pattern of Figure 1A(c). Thus, the pattern implies the exfoliation of the layered structure. The Tyndall light scattering (Figure 1D) indicates the presence of colloidal species. The high peak intensity of the (00*l*) planes at 16.72, 8.36, and 5.58 Å for the TMA^+-intercalated sample indicates that the layered structure is well-retained, coinciding with the SEM image [Figure 1C(b)], even though the sample was treated under the hydrothermal condition. But it should be pointed out that the mechanical force in the exfoliation process may break down the nanosheets, as observed for other kinds of nanosheets.[49,50]

3.2. Formation Condition of Anatase TiO_2. The products obtained through the hydrothermal treatment of the nanosheets were subjected to XRD measurement (see Supporting Information, Figures S1–S4). Some typical patterns are given in Figure 2A; the identified phases are summarized in Table 2. As shown, anatase, rutile, and brookite phases are formed, depending on pH and temperature. The same as found in our previous works using different precursors,[41] the rutile phase formed at low pH (0.5 in the present case) within the temperature range; the brookite phase, at high pH; and the anatase phase, at pH values between them. But the temperature

DOI: 10.1021/acsami.5b00227
ACS Appl. Mater. Interfaces 2015, 7, 7995–8004

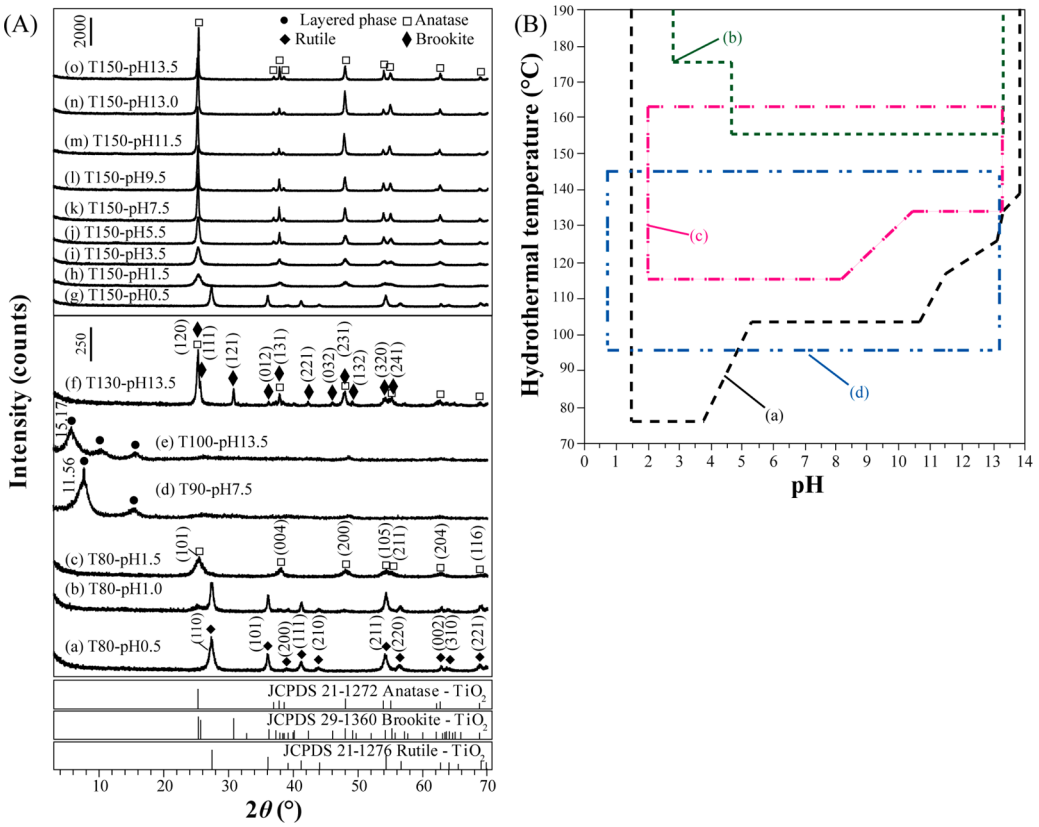

Figure 2. (A) Typical XRD patterns for samples obtained from the metatitanic nanosheets. (B) The formation area of anatase phase in (a) the current work, compared with the works using different precursors of (b) $H_2Ti_4O_9$ nanoribbons,[41] (c) *n*-propylamine-intercalated $H_{1.07}Ti_{1.73}O_4$ nanosheets,[51] and (d) TBA^+-intercalated $H_{1.07}Ti_{1.73}O_4$ nanosheets.[24]

Table 2. Dependences of the Crystalline Phases on the Hydrothermal Temperature and pH Adjusted for the Metatitanic Nanosheet Colloidal Suspension[a]

pH	80 °C	90 °C	100 °C	110 °C	120 °C	130 °C	140 °C	150 °C	160 °C	170 °C	180 °C
0.5	R	R	R	R	R	R	R	R	R	R	R
1.0	A + R	A + R	A + R	A + R	A + R	A + R	—	—	A + R	A + R	A + R
1.5	A	A	A	A	A	A	A	A	A	A	A
3.5	A	A	A	A	A	A	A	A	A	A	A
5.5	A + L	A + L	A + L	A	A	A	A	A	A	A	A
7.5	–	L	A + L	A	A	A	A	A	A	A	A
9.5	–	–	–	A	A	A	A	A	A	A	A
11.5	–	–	–	A + L	A	A	A	A	A	A	A
13.0	–	–	–	A + B	A + B	A	A	A	A	A	A
13.5	–	–	L	–	A + B	A + B	A	A	A	A	A

[a]A, anatase phase (tetragonal symmetry, space group $I4_1/amd$, JCPDS No. 21-1272); B, brookite phase (orthorhombic symmetry, space group *Pcab*, JCPDS No. 29-1360); R, rutile phase (tetragonal symmetry, space group $P4_2/mnm$, JCPDS No. 21-1276); L, unreacted layered compound.

range (110−130 °C, at pH >11.5) for the formation of the brookite phase is lower than that (T > 170 °C at pH 14) in the case of $H_2Ti_4O_9$ nanoribbon precursor. In Figure 2B, the formation area of the anatase is enlarged; the single phase can be obtained even at a low pH of 1.5−3.5 and 80 °C. The differences in anatase area indicate that the formation of anatase is strongly dependent on the precursors, and the metatitanic nanosheets transform more easily to anatase than other precursors.

At an initial temperature, with the increase of pH the diffraction peaks of anatase became strong and sharp, implying an increase of crystallinity [Figure 2A(h−o)]; with the increase of temperatures, the crystallinity of the anatase crystals (e.g., at pH 1.5) increases (see Figure S2A in the Supporting Information), but the lattice parameters are not found to change markedly (a = 0.377 and c = 0.950 nm).

The unreacted layered compound was found at pH ≥5.5 and low temperatures (Table 2). The basal spacing of the layered structures decreases with a decrease of pH [Figures 2A(d,e) and S3 and S4, Supporting Information] from 15.2 Å (pH 13.5) to 11.6 Å (pH 7.5) and 11.3 Å (pH 5.5). This implies the restacking of the metatitanic nanosheets. The decrease in basal spacing could be produced by the decrease of TMA^+ ions due to the decrease of pH, and even the 11.3 Å value is close to the value of a monolayer layer of TMA^+ ions in the interlayer space (4.60 Å of the layer thickness + 5.30 Å of TMA^+ = 10.90 Å). The decrease of TMA^+ in the interlayer space may be caused by

DOI: 10.1021/acsami.5b00227
ACS Appl. Mater. Interfaces 2015, 7, 7995−8004

the H^+/TMA^+ ion-exchange reaction in the hydrochloric acid solution.

3.3. Morphology of Anatase TiO_2. Figure 3 shows the typical FE-SEM images of the samples. The T130-pH0.5 sample exhibits rodlike particle morphology constructed from nanorodlike crystals, which correspond to rutile particles (Figure 3a). The T170-pH1.0 sample shows some bigger rodlike particle morphology and a lot of smaller irregular particle morphology (Figure 3b), which is the mixed phase of rutile and anatase [Figure S1B(h) in the Supporting Information]. The smaller irregular particles correspond to the anatase phase and the bigger rodlike particles with the length of about 100 nm and the thickness of about 20 nm correspond to the rutile phase (Figure 5c,d). For T100-pH1.5, nanorodlike and other irregularly shaped anatase nanocrystals with the size of about several nanometers were observed (Figure 3c), and after hydrothermal treatment at 180 °C, the size of the nanorodlike particles increased to about 15 nm in length and the morphologies also remained (Figure 3d), indicating the increase of crystallinity. At pH ≥3.5, short and long spindle-shaped anatase nanocrystals were observed, and the size of the spindle increased with the increase of the hydrothermal temperature (comparing parts f and g of Figure 3) and the pH of the reaction solution (comparing parts g–j of Figure 3), implying that the growth of the spindle nanocrystals is faster at higher temperatures and pH. Furthermore, to our surprise, many fringes are found on the surface of the spindle-shaped nanocrystals, which are parallel to the short axis direction ([010] direction) and perpendicular to the long axis direction ([001] direction) of the spindle, respectively, indicating that the spindle-shaped nanocrystals possibly grow along the *c*-axis direction of the crystal (Figure 3f–j). The T130-pH13.5 sample is a mixed phase of anatase and brookite [Figure 2A(f)], and the morphology of the particles with a rough surface could be clearly observed by FE-SEM (Figure 3k). Figure 3k further reveals that the irregularly shaped particles predominantly 200–500 nm in length are made up of nanocrystal subunits. Since the main phase in this sample is brookite, the irregularly shaped particles can be assigned to the brookite phase. The T150-pH13.5 sample exhibits two kinds of typical anatase particle morphologies, the smaller spindle-shaped particle morphology about 250 nm in length and 30 nm in width and the larger cone-shaped morphology with a length of about 500 nm (Figure 3l). The smaller spindle-shaped particles are formed by a mechanism similar to that of T160-pH11.5, while the larger cone-shaped particles may be formed by a structural transformation reaction from brookite particles that have similar particle size (Figure 3k).

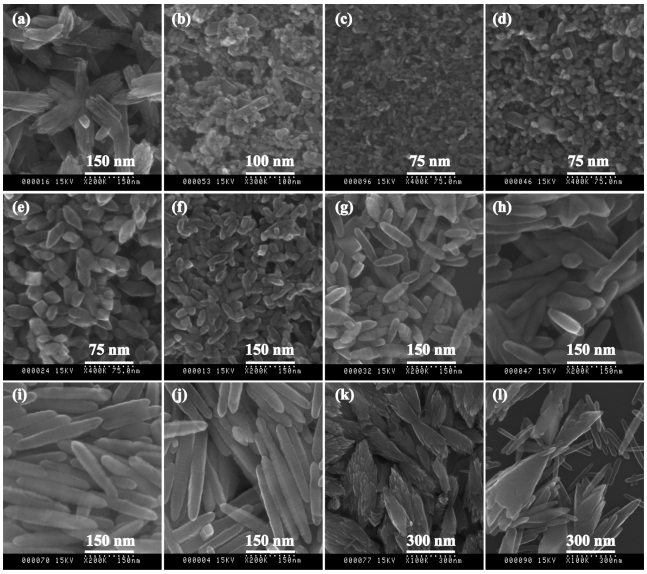

Figure 3. FE-SEM images of (a) T130-pH0.5 (rutile phase), (b) T170-pH1.0 (rutile and anatase phases), (c) T100-pH1.5 (anatase phase), (d) T180-pH1.5 (anatase phase), (e) T170-pH3.5 (anatase phase), (f) T140-pH5.5 (anatase phase), (g) T160-pH5.5 (anatase phase), (h) T160-pH7.5 (anatase phase), (i) T160-pH9.5 (anatase phase), (j) T160-pH11.5 (anatase phase), (k) T130-pH13.5 (anatase and brookite phases), and (l) T150-pH13.5 (anatase phase).

3.4. Exposed Facets of Nanocrystals. Figure 4a is the TEM images of the nanorod anatase obtained at pH 1.5. The unparalleled lattice fringes of 3.51 Å with the angle of 82° can be indexed to the (101) and (011) planes of anatase. The angle between (101) and (011) of 82° agrees well with the theoretical value 82.1°, according to calculated result from the lattice constants of anatase (tetragonal, space group $I4_1/amd$, JCPDS 21-1272, $Z = 4$, $a = 3.7852$ Å, and $c = 9.5139$ Å).[52] Since a crystal plane perpendicular to two planes is uncertain, the exposed crystal facets are expressed as [111] facets.

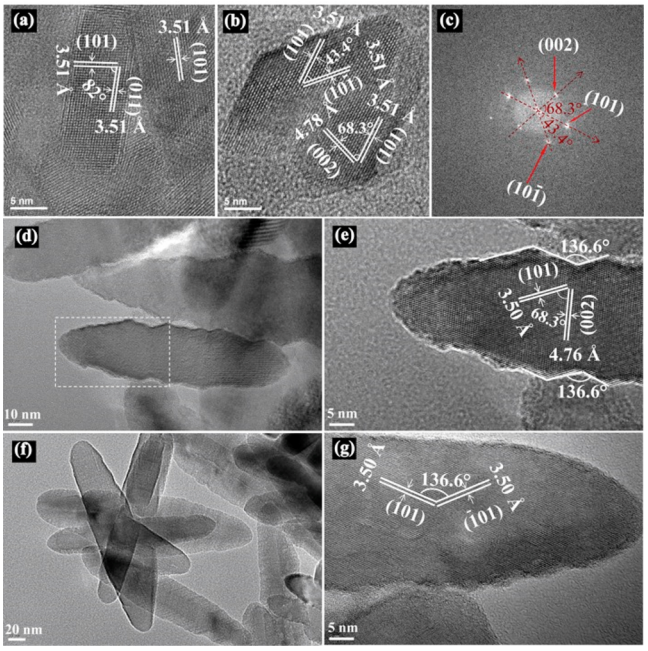

Figure 4. TEM images of (a) T180-pH1.5, (b) T170-pH3.5, (d, e) T160-pH5.5, and (f, g) T160-pH7.5 and (c) the fast Fourier-transform diffraction pattern of part b. All these samples are anatase phase.

For the short spindle-shaped anatase nanocrystals, taking T170-pH3.5 as an example, TEM observations (Figure 4b) reveal three sets of lattice fringes with spacing of 3.51, 3.51, and 4.78 Å, which can be indexed to (101), (10$\bar{1}$), and (002) planes of anatase, respectively. The angles indicated in the corresponding fast Fourier-transform diffraction pattern (Figure 4c) are 68.3° and 43.4°, which are identical to the theoretical values obtained from the angles between (101) and (002) planes and between (101) and (10$\bar{1}$) planes, respectively. Therefore, the short spindle-shaped anatase nanocrystals preferentially expose the {010} facets on their basal plane

DOI: 10.1021/acsami.5b00227
ACS Appl. Mater. Interfaces 2015, 7, 7995–8004

and four side faces corresponding to {101} facets. The TEM images (Figure 4d–g) for the long spindle-shaped anatase obtained in the pH range of 5.5–13.5 also show the lattice fringe with *d*-spacing values of 3.50, and 4.76 Å, corresponding to (101) and (002) planes of the anatase phase, respectively (Figure 4e). Observed through the [010] zone axis, the (101) and (002) planes of anatase have an interfacial angle of 68.3°, similar to the theoretical value (68.3°). Figure 4g shows two sets of lattice fringes, both with spacing of 3.50 Å, which can be indexed to (101) and ($\bar{1}$01) crystal planes of the anatase phase, respectively. The angle between them is 136.6°, identical to the theoretical value obtained from the angles between the (101) and ($\bar{1}$01) planes.

It can be concluded that the small anatase crystals of the nanorods obtained at low pH have the exposed [111] facets, while the large spindle-shaped ones (short and long) have the exposed {010} facets. The results are similar as those we reported for the precursor of $H_2Ti_4O_9$ nanoribbons, though for the latter the range of pH values and temperatures for which the formation occurs is small (Figure 2B).

Figure 5a,b shows the TEM images of the rodlike rutile crystals. The lattice fringe has *d*-spacing values of 3.25 and 3.00

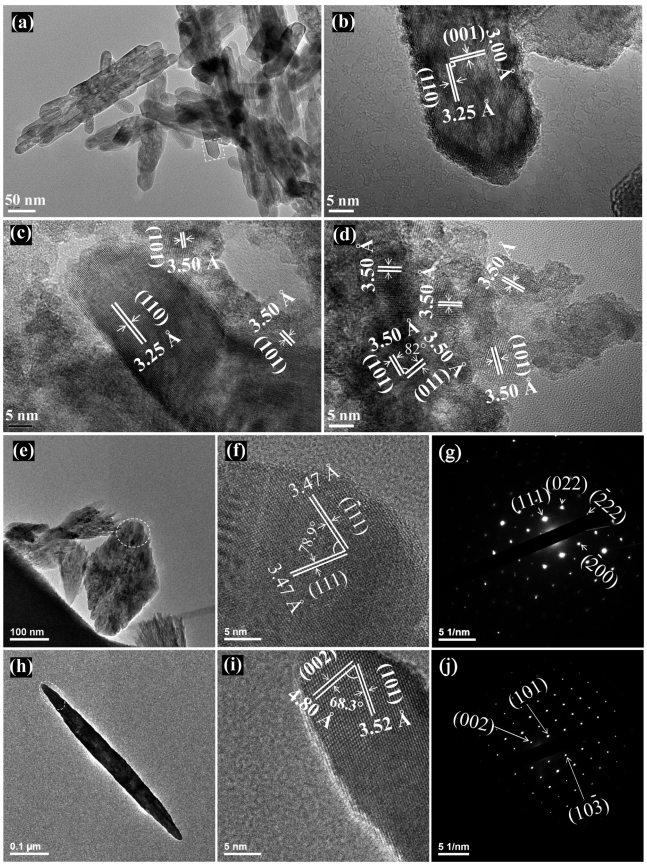

Figure 5. TEM images of (a, b) T180-pH0.5 (rutile phase), (c, d) T170-pH1.0 (rutile and anatase phases), (e, f) T130-pH13.5 (anatase and brookite phases), and (h, i) T150-pH13.5 (anatase phase) and SAED pattern of (g) T130-pH13.5 and (j) T150-pH13.5.

Å, corresponding to the (110) and (001) planes of rutile TiO_2, respectively, and the angle between the two planes is 90°. That is, the long axis of the rodlike crystal corresponds to the *c*-axis direction of the rutile structure and the lateral exposed crystal facets are {110} facets.[53] In Figure 5c,d, some larger rodlike particles and small nanorod particles are observed. The lattice fringes in the TEM images indicate clearly that they are {110}-facet-exposed rutile phase in the lateral part of the crystals (Figure 5c) and [111]-facet-exposed anatase (Figure 5d) crystals, respectively.

Figure 5f exhibits two types of lattice fringes with spacing of 3.47 and 3.47 Å, which can be indexed to the (111) and ($\bar{1}$11) crystal planes of the brookite phase, respectively, and the angle between them is 78.9°, which is well consistent with the theoretical value of 78.9°. The SAED pattern in Figure 5g further confirms that the particles with an irregular profile are brookite. Figure 5h exhibits a typical TEM image of a spindle-shaped single nanocrystal, the fringe spacings of 3.52 and 4.80 Å corresponding to the (101) and (002) planes of anatase, and the angle between the (101) and (002) planes is 68.3°. The corresponding SAED pattern (Figure 5j) further confirms that the spindle-shaped crystal is a single nanocrystal, and the zone axis is indexed to be the [010] direction.

3.5. Transformation Reaction Mechanism and Exposure Rate of {010} Facets. TMA^+-intercalated metatitanic acid is exfoliated into elementary host nanosheets, which have cavities within the layers. The transformation of metatitanic nanosheets to anatase can be described as reaction 1

$$[TiO_3]^{2-} \rightarrow TiO_2 + O^{2-} \quad (1)$$

or in the acidic and alkaline solutions, the reactions are 1a and 1b, respectively

$$[TiO_3]^{2-} + 2H^+ \rightarrow TiO_2 + H_2O \quad (1a)$$

$$[TiO_3]^{2-} + H_2O \rightarrow TiO_2 + 2OH^- \quad (1b)$$

The reaction releases oxygen ions, and reaction 1 implies that the release of oxygen ion occurs in each TiO_6 octahedron. As shown in Table 2, higher acidity is beneficial for reaction 1; i.e., reaction 1a takes place at a lower temperature than reaction 1b. In other words, reaction 1a is kinetically faster than reaction 1b. Thus, higher acidity is helpful to the release of oxygen, and the large amount of released oxygen ions produces small oligomer fragments of TiO_6 octahedron, which recrystallized into TiO_2 nanocrystals via the stacking of the fragments, leading to the formation of TiO_2 crystals at lower temperatures than for the others precursors (Figure 2B). At higher pH, the reaction 1b takes place, as it proceeds more difficultly than reaction 1a. Higher temperature is necessary for the transformation. However, it is more important that pH influences the crystal morphology. For the nanorod and short- and long spindle-shaped anatase crystals, the crystal shapes (on the left for each pH in Figure 6) simulated by using the VESTA[54] software (details in Supporting Information) agree well with the FE-SEM images (on the right for each pH in Figure 6). For spindle-shaped anatase nanocrystals, a similar layer-upon-layer, stacked structure was observed along the [001] direction of the anatase nanocrystals.

The amount of released oxygen ions is more than for the precursors of $[Ti_{1.73}O_4]^{1.07-}$ nanosheets ($[TiO_{2.31}]^{0.62-} \rightarrow TiO_2 + 0.31O^{2-}$) and $[Ti_4O_9]^{2-}$ nanoribbon ($[TiO_{2.25}]^{0.5-} \rightarrow TiO_2 + 0.25O^{2-}$) per titanium atom. For the latter two precursors, the crystalline transformation takes place via in situ topotactic reactions,[48,55] but the crystalline transformation in the present case is different from the normal topotactic reaction. Because of the cavities within the nanosheet, such a nanosheet can be split easily into smaller oligomer fragments, and the H_2TiO_3

DOI: 10.1021/acsami.5b00227
ACS Appl. Mater. Interfaces 2015, 7, 7995–8004

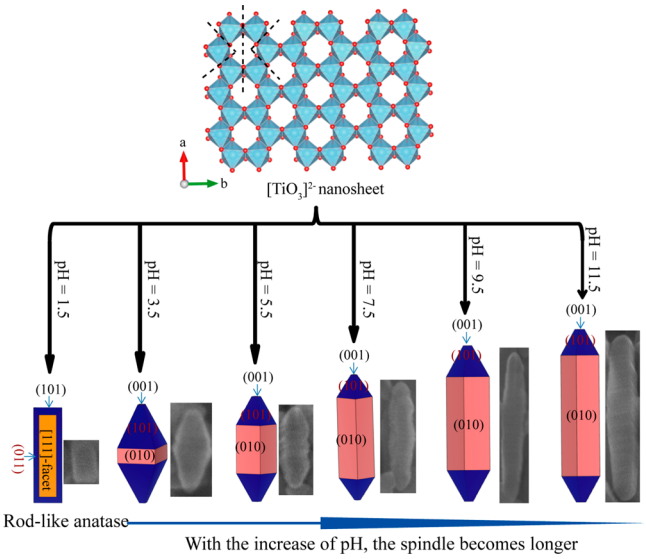

Figure 6. Transformation reaction mechanism from layered metatitanic lithium oxides to anatase TiO_2 nanocrystal and simulated crystalline shapes.

nanosheet crystal is split easily to small, primarily TiO_6 octahedral oligomer fragments along the edge-shared oxygen atoms. These fragments recrystallize, forming anatase crystal. Namely, the H_2TiO_3 nanosheets are transformed to TiO_2 mainly via the dissolution−recrystallization process, but the dissolved particles are the oligomer fragments, which are smaller than those from the other mentioned precursors. The formation of rutile via the dissolution−recrystallization process was also observed in previous work on the $[Ti_4O_9]^{2-}$ nanoribbon and $[Ti_{1.73}O_4]^{1.07-}$ nanosheet precursors.[24,41] This dissolution (to the fragments)−recrystallization (through the fragments) causes the formation of rutile with large, rodlike particle morphology and smaller, irregular anatase nanoparticles at low pH, and the fragments stack along the [001] direction of the anatase crystal with {010}-faceted side faces and the long axis in the [001] direction at high pH. With increasing pH, the stacking topotactic structural transformation mechanism becomes predominant. This is the reason why the spindle becomes longer with the increase of the pH value (compare part g with parts h−j of Figure 3). Furthermore, the anatase phase is unstable under the low pH conditions and transforms easily to the stable rutile phase. Such small fragments are disadvantageous for the brookite formation, whereas the fragments of $[Ti_4O_9]^{2-}$ nanoribbons and $[Ti_{1.73}O_4]^{1.07-}$ nanosheets are not, as observed previously at low pH.[41,56] The H_2TiO_3 nanosheets become stable with increasing pH value. In other words, the dissolved fragments/particles contain more TiO_6 octahedrons. The fragments first transform into the brookite phase with large particle size at low temperature, and then the brookite phase transformed into the anatase phase at higher temperature because the anatase phase is more stable than the brookite phase. Therefore, the spindle anatase nanocrystals are formed preferentially in the pH range from 1.0 to 11.5. The increase of the length of the spindle anatase nanocrystals with increasing pH can be also explained by the increase of the stability of the H_2TiO_3 nanosheets in the reaction solution.

In summary, the transformation from the H_2TiO_3 nanosheet crystal to TiO_2 nanocrystals is mainly via the dissolution−recrystallization process, but the size of the dissolved fragments increases with increasing pH; at higher pH, the "recrystallization" proceeds via the mechanism of the stacking topotactic structural transformation from the larger fragments.

The different aspect ratios of the spindle result in the different ratios of {010} to the other facets. The percentage of {010} facets for the spindle-shaped anatase can be calculated according to the approximate equation

$$S_{\{010\}}\% = \frac{S_{\{010\}}}{S_{\{010\}} + S_{\{101\}}}$$

where $S_{\{010\}}$ and $S_{\{101\}}$ are the surface areas of {010} and {101} facets, respectively. The detailed calculation for the estimation of the percentage of exposed {010} facets for the spindle are shown in Figure S8 and Table S2 (see the Supporting Information). As shown in Figure 7, the exposure rate of {010}

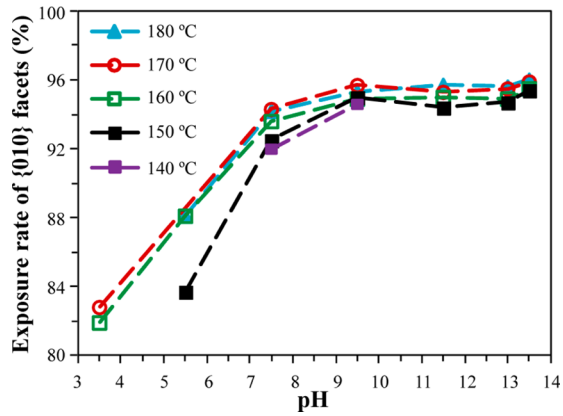

Figure 7. The exposure rate of {010} facets of spindle-shaped anatase nanocrystals changes at different pH values and temperatures.

facets of spindle-shaped anatase nanocrystals increases drastically before pH ≤7.5 to about 90% and then slowly as pH increases to ≥9.5 for all temperatures. The values for 170 and 180 °C have almost the same curves, but are higher than the others. A {010}-facet-exposure ratio of 96% can be achieved by the present synthesis process.

3.6. Photocatalytic Activities. To evaluate the photocatalytic performance of the products, four typical samples (T180-pH1.5, T170-pH3.5, T160-pH5.5, T160-pH7.5) were selected for the photocatalytic decomposition of MB. The temporal evolution of the spectral changes accompanying the photodegradation of MB over the prepared T160-pH5.5 nanocrystals is shown in Figure 8a. The intensity of the maximal absorption peak at 670 nm decreased with the increase of irradiation time, indicating photodegradation of the MB aqueous solution. The blue-shift of the absorption peak at 670 nm in the UV−visible absorption is also observed during the course of the photodegradation, implying the N-demethylation of MB.[57] Thus, photodecolorization of chromogenic groups and dissociation of methyl occurred simultaneously.

The time-dependent photodegradation of MB was used to examine the photocatalytic activities of the TiO_2 nanocrystals, as shown in Figure 8b. MB degrades a little in the absence of catalyst, and the η values increase in the order of 6.1% (without catalyst), 61.3% (T180-pH1.5), 67.2% (Degussa P25), 78.9% (T160-pH7.5), 82.0% (T160-pH5.5), and 85.5% (T170-pH3.5), under UV irradiation of 60 min.

DOI: 10.1021/acsami.5b00227
ACS Appl. Mater. Interfaces 2015, 7, 7995−8004

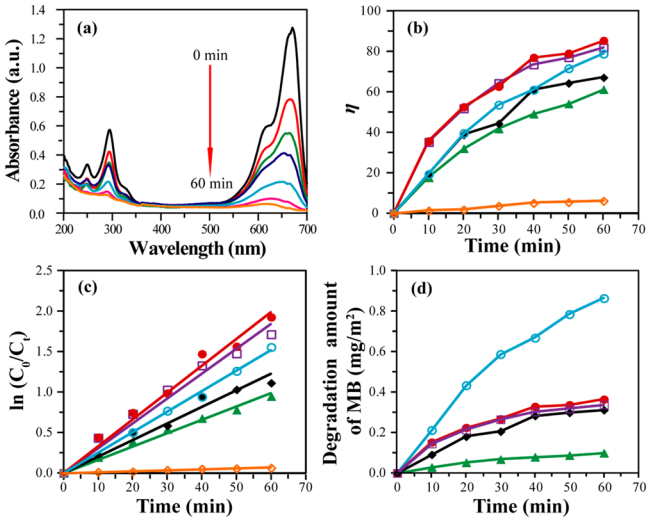

Figure 8. (a) UV−visible absorption spectra changes of methylene blue (MB) solution as a function of irradiation time in the presence of T160-pH5.5 nanocrystals catalyst. (b) Time-dependent photodegradation of MB under UV illumination in the presence and absence of catalysts. (c) Kinetic plots of photocatalytic degradation of 1.56×10^{-5} mol L^{-1} MB solution using different TiO_2 nanocrystals under UV irradiation. (d) Degradation amount of MB [MB (mg)/S_{BET} (m^2) of TiO_2]. Key: solid red circle, T170-pH3.5; open purple square, T160-pH5.5; open blue circle, T160-pH7.5; solid black diamond, Degussa P25; solid green triangle, T180-pH1.5; open orange diamond, without catalyst).

The kinetic plots of the photocatalytic degradation of MB solution are shown in Figure 8c. The apparent rate constants (k_{app}) of the samples, the blank (without catalyst), T180-pH1.5, Degussa P25, T160-pH7.5, T160-pH5.5, and T170-pH3.5 were estimated to be 0.0011, 0.0164, 0.0204, 0.0252, 0.0308, and 0.0332 min^{-1}, respectively. The value of k_{app} for T170-pH3.5 exhibits the highest photocatalytic activity among the samples, being 1.08, 1.32, 1.63, 2.02, and 30.18 times greater than that of T160-pH5.5, T160-pH7.5, Degussa P25, T180-pH1.5, and the blank, respectively. The k_{app} value changes in the order T170-pH3.5 > T160-pH5.5 > T160-pH7.5 > Degussa P25 > T180-pH1.5.

It is well-known that the photocatalytic activity is closely related with the particle morphology, crystallinity, and particle size; especially, the surface area and crystal facets have been found to play a crucial role in the photocatalytic activity of TiO_2 nanocrystals.[58] Among the samples with dominant {010} facets, the photocatalytic activity is ranked in the order of T160-pH7.5 < T160-pH5.5 < T170-pH3.5, which is consistent with the increasing order of the S_{BET} (see Table S1 in Supporting Information). For Degussa P25, the anatase phase contains two types of particle morphology, one is near-spherical morphology (~40%) without a specific facet on the crystal surface, and the other is tetragonal morphology (~40%) with specific [111] facets on the crystal surface.[56] Degussa P25 exhibits a photocatalytic activity less than those of T70-pH3.5, T160-pH5.5, and T160-pH7.5, suggesting that the photoactivity of the {010} facet is higher than that without a specific exposed facet and the [111] facet. T180-pH1.5 shows the lowest photocatalytic activity, although it has exposed active [111] facets and the largest surface area (see Table S1 in the Supporting Information). This result may be caused by two facts, one is the heterojunction of anatase/rutile (Degussa P25), which enhanced the photocatalytic activity of TiO_2,[59] and the other is the loose and random states of intra-aggregate mesopores and the lower crystallinity of the T180-pH1.5, which exaggerate the photoexcited electron−hole recombination rate.[60,61] In addition, because the prepared TiO_2 nanocrystals have different specific surface areas, to estimate the intrinsic photocatalytic efficiency of TiO_2, the degradation ratios of MB per unit surface area of catalyst were compared (Figure 8d). The degradation ratios at 60 min were 0.10, 0.31, 0.34, 0.36, and 0.86 mg/m^2 for T180-pH1.5, Degussa P25, T160-pH5.5, T170-pH3.5, and T160-pH7.5, respectively. Degussa P25 exhibits higher degradation ratios than T180-pH1.5, attributed to the heterojunction of anatase/rutile. These results suggest that the higher photocatalytic activity is mainly due to the exposed {010} facets on their surface, which have both a favorable surface atomic structure and a surface electronic structure.[11,22] Therefore, the photocatalytic activity of the nanocrystals is ranked in the order of [111] facet < {010} facet.

4. CONCLUSIONS

The lithium ions in lithium metatitanate (Li_2TiO_3) with the rock-salt structure can be entirely extracted through HCl treatment. The protonated sample obtained has low basal spacing, while the crystal morphology is retained. The crystals delaminated to $[TiO_3]^{2-}$ nanosheets with cavities within the layers, after the protonated metatitanic oxide was intercalated by TMA^+. During hydrothermal treatment, the nanosheet can transform to TiO_2 according to the reaction of $[TiO_3]^{2-} \rightarrow TiO_2 + O^{2-}$. Greater oxygen release from the precursor than from $[Ti_4O_9]^{2-}$ nanoribbon and $[Ti_{1.73}O_4]^{1.07-}$ nanosheet leads to a broadened pH−temperature area of the transformation. Low pH fosters the [111]-facet-exposed anatase TiO_2 nanorods, whereas the increase of pH is benefit to the higher exposure of the {010} facet anatase crystal, relative to those of {001} and {101}, leading to morphology changes from short spindle (pH 3.5) to long spindle ($5.5 \leq pH \leq 13.5$). The anatase nanocrystals with more exposed {010} facets exhibited higher photodegradation efficiency toward MB.

■ ASSOCIATED CONTENT

Supporting Information

XRD patterns of the samples obtained by hydrothermal treatment of metatitanic nanosheet suspension at various temperatures and pH conditions; TG−DTA curves of the samples obtained at pH 5.5; particle size, surface area, and pore distributions; the calculation of facets percentage of {010} spindle-shaped sample; and the detailed calculated values of the spindle-shaped anatase TiO_2 nanocrystals. This material is available free of charge via the Internet at http://pubs.acs.org.

■ AUTHOR INFORMATION

Corresponding Authors

*Q.F.: e-mail, feng@eng.kagawa-u.ac.jp; fax, +81-87-864-2438; tel, +81-87-864-2402.

*X.Y.: e-mail, yang.xiaojing@bnu.edu.cn; fax, +86-10-5880-2075; tel, +86-10-5880-2960.

Notes

The authors declare no competing financial interest.

DOI: 10.1021/acsami.5b00227
ACS Appl. Mater. Interfaces 2015, 7, 7995−8004

■ ACKNOWLEDGMENTS

This work was supported by the National Science Foundation of China (Grants. 51272030) and by Grants-in-Aid for Scientific Research (B) (Grants. 23350101) from the Japan Society for the Promotion of Science.

■ REFERENCES

(1) Jun, Y. W.; Choi, J. S.; Cheon, J. Shape Control of Semiconductor and Metal Oxide Nanocrystals through Nonhydrolytic Colloidal Routes. *Angew. Chem., Int. Ed.* **2006**, *45*, 3414−3439.
(2) Wang, C.; Daimon, H.; Onodera, T.; Koda, T.; Sun, S. H. A General Approach to the Size- and Shape-Controlled Synthesis of Platinum Nanoparticles and Their Catalytic Reduction of Oxygen. *Angew. Chem., Int. Ed.* **2008**, *47*, 3588−3591.
(3) Tao, A. R.; Habas, S.; Yang, P. D. Shape Control of Colloidal Metal Nanocrystals. *Small* **2008**, *4*, 310−325.
(4) Tian, N.; Zhou, Z. Y.; Sun, S. G.; Ding, Y.; Wang, Z. L. Synthesis of Tetrahexahedral Platinum Nanocrystals with High-Index Facets and High Electro-Oxidation Activity. *Science* **2007**, *316*, 732−735.
(5) Jiang, Z. Y.; Kuang, Q.; Xie, Z. X.; Zheng, L. S. Syntheses and Properties of Micro/Nanostructured Crystallites with High-Energy Surfaces. *Adv. Funct. Mater.* **2010**, *20*, 3634−3645.
(6) Liu, B.; Khare, A.; Aydil, E. S. TiO_2-B/Anatase Core-Shell Heterojunction Nanowires for Photocatalysis. *ACS Appl. Mater. Interfaces* **2011**, *3*, 4444−4450.
(7) Yang, H. G.; Sun, C. H.; Qiao, S. Z.; Zou, J.; Liu, G.; Smith, S. C.; Cheng, H. M.; Lu, G. Q. Anatase TiO_2 Single Crystals with a Large Percentage of Reactive Facets. *Nature* **2008**, *453*, 638−642.
(8) Yang, H. G.; Liu, G.; Qiao, S. Z.; Sun, C. H.; Jin, Y. G.; Smith, S. C.; Zou, J.; Cheng, H. M.; Lu, G. Q. Solvothermal Synthesis and Photoreactivity of Anatase TiO_2 Nanosheets with Dominant {001} Facets. *J. Am. Chem. Soc.* **2009**, *131*, 4078−4083.
(9) Wen, P. H.; Tao, Z. Q.; Ishikawa, Y.; Itoh, H.; Feng, Q. Dye-Sensitized Solar Cells Based on Anatase TiO_2 Nanocrystals Exposing Specific Lattice Plane on the Surface. *Appl. Phys. Lett.* **2010**, *97*, 131906.
(10) Li, J. M.; Xu, D. S. Tetragonal Faceted-Nanorods of Anatase TiO_2 Single Crystals with a Large Percentage of Active {100} Facets. *Chem. Commun.* **2010**, *46*, 2301−2303.
(11) Pan, J.; Wu, X.; Wang, L. Z.; Liu, G.; Lu, G. Q.; Cheng, H. M. Synthesis of Anatase TiO_2 Rods with Dominant Reactive {010} Facets for the Photoreduction of CO_2 to CH_4 and Use in Dye-Sensitized Solar Cells. *Chem. Commun.* **2011**, *47*, 8361−8363.
(12) Zhang, H. M.; Wang, Y.; Liu, P. R.; Han, Y. H.; Yao, X. D.; Zou, J.; Cheng, H. M.; Zhao, H. J. Anatase TiO_2 Crystal Facet Growth: Mechanistic Role of Hydrofluoric Acid and Photoelectrocatalytic Activity. *ACS Appl. Mater. Interfaces* **2011**, *3*, 2472−2478.
(13) Wang, L.; Zang, L.; Zhao, J. C.; Wang, C. Y. Green Synthesis of Shaped-Defined Anatase TiO_2 Nanocrystals Wholly Exposed with {001} and {100} Facets. *Chem. Commun.* **2012**, *48*, 11736−11738.
(14) Li, J. M.; Cao, K.; Xu, D. S. Tetragonal Faceted-Nanorods of Anatase TiO_2 with a Large Percentage of Active {100} Facets and Their Hierarchical Structure. *CrystEngComm* **2012**, *14*, 83−85.
(15) Liao, Y. L.; Zhang, H. W.; Que, W. X.; Zhong, P.; Bai, F. M.; Zhong, Z. Y.; Wen, Q. Y.; Chen, W. H. Activating the Single-Crystal TiO_2 Nanoparticle Film with Exposed {001} Facets. *ACS Appl. Mater. Interfaces* **2013**, *5*, 6463−6466.
(16) Zhao, J.; Zou, X. X.; Su, J.; Wang, P. P.; Zhou, L. J.; Li, G. D. Synthesis and Photocatalytic Activity of Porous Anatase TiO_2 Microspheres Composed of {010}-Faceted Nanobelts. *Dalton Trans.* **2013**, *42*, 4365−4368.
(17) Nunzi, F.; Storchi, L.; Manca, M.; Giannuzzi, R.; Giglin, G.; Angelis, F. D. Shape and Morphology Effects on the Electronic Structure of TiO_2 Nanostructures: From Nanocrystals to Nanorods. *ACS Appl. Mater. Interfaces* **2014**, *6*, 2471−2478.
(18) Li, W.; Liu, C.; Zhou, Y. X.; Bai, Y.; Feng, X.; Yang, Z. H.; Lu, L. H.; Lu, X. H.; Chan, K. Y. Enhanced Photocatalytic Activity in Anatase/TiO_2(B) Core-Shell Nanofiber. *J. Phys. Chem. C* **2008**, *112*, 20539−2.545.
(19) Kubacka, A.; Fernández-García, M.; Colón, G. Advanced Nanoarchitectures for Solar Photocatalytic Applications. *Chem. Rev.* **2012**, *112*, 1555−1614.
(20) Ong, W. J.; Tan, L. L.; Chai, S. P.; Yong, S. T.; Mohamed, A. R. Highly Reactive {001} Facets of TiO_2-Based Composites: Synthesis, Formation Mechanism and Characterization. *Nanoscale* **2014**, *6*, 1946−2008.
(21) Lazeri, M.; Vittadini, A.; Selloni, A. Structure and Energetics of Stoichiometric TiO_2 Anatase Surfaces. *Phys. Rev. B* **2001**, *63*, 155409.
(22) Pan, J.; Liu, G.; Lu, G. Q.; Cheng, H. M. On the True Photoreactivity Order of {001}, {010}, and {101} Facets of Anatase TiO_2 Crystals. *Angew. Chem., Int. Ed.* **2011**, *50*, 2133−2137.
(23) Ohno, T.; Sarukawa, K.; Matsumura, M. Crystal Faces of Rutile and Anatase TiO_2 Particles and Their Roles in Photocatalytic Reactions. *New J. Chem.* **2002**, *26*, 1167−1170.
(24) Wen, P. H.; Itoh, H.; Tang, W. P.; Feng, Q. Single Nanocrystals of Anatase-Type TiO_2 Prepared from Layered Titanate Nanosheets: Formation Mechanism and Characterization of Surface Properties. *Langmuir* **2007**, *23*, 11782−11790.
(25) Han, X. G.; Kuang, Q.; Jin, M. S.; Xie, Z. X.; Zheng, L. S. Synthesis of Titania Nanosheets with a High Percentage of Exposed (001) Facets and Related Photocatalytic Properties. *J. Am. Chem. Soc.* **2009**, *131*, 3152−3153.
(26) Dinh, C.-T.; Nguyen, T.-D.; Kleitz, F.; Do, T.-O. Shape-Controlled Synthesis of Highly Crystalline Titania Nanocrystals. *ACS Nano* **2009**, *3*, 3737−3743.
(27) Han, X. G.; Wang, X.; Xie, S. F.; Kuang, Q.; Ouyang, J. J.; Xie, Z. X.; Zheng, L. S. Carbonate Ions-Assisted Syntheses of Anatase TiO_2 Nanoparticles Exposed with High Energy (001) Facets. *RSC Adv.* **2012**, *2*, 3251−3253.
(28) Xie, S. F.; Han, X. G.; Kuang, Q.; Fu, J.; Zhang, L.; Xie, Z. X.; Zheng, L. S. Solid State Precursor Strategy for Synthesizing Hollow TiO_2 Boxes with a High Percentage of Reactive {001} Facets Exposed. *Chem. Commun.* **2011**, *47*, 6722−6724.
(29) Yu, Y. L.; Wang, X. L.; Sun, H. Y.; Ahmad, M. 3D Anatase TiO_2 Hollow Microspheres Assembled with High-Energy {001} Facets for Lithium-Ion Batteries. *RSC Adv.* **2012**, *2*, 7901−7905.
(30) Wu, L.; Yang, B. X.; Yang, X. H.; Chen, Z. G.; Li, Z.; Zhao, H. J.; Gong, X. G.; Yang, H. G. On the Synergistic Effect of Hydrohalic Acids in the Shape-Controlled Synthesis of Anatase TiO_2 Single Crystals. *CrystEngComm* **2013**, *15*, 3252−3255.
(31) Feng, J. Y.; Yin, M. C.; Wang, Z. Q.; Yan, S. C.; Wan, L. J.; Li, Z. S.; Zou, Z. G. Facile Synthesis of Anatase TiO_2 Mesocrystal Sheets with Dominant {001} Facets Based on Topochemical Conversion. *CrystEngComm* **2010**, *12*, 3425−3429.
(32) Lai, Z. C.; Peng, F.; Wang, Y.; Wang, H. J.; Yu, H.; Liu, P. R.; Zhao, H. J. Low Temperature Solvothermal Synthesis of Anatase TiO_2 Single Crystals with Wholly {100} and {001} Faceted Surfaces. *J. Mater. Chem.* **2012**, *22*, 23906−23912.
(33) Wang, Z. Y.; Huang, B. B.; Dai, Y.; Liu, Y. Y.; Zhang, X. Y.; Qin, X. Y.; Wang, J. P.; Zheng, Z. K.; Cheng, H. F. Crystal Facets Controlled Synthesis of Graphene@TiO_2 Nanocomposites by a One-Pot Hydrothermal Process. *CrystEngComm* **2012**, *14*, 1687−1692.
(34) Zhou, X. S.; Peng, F.; Wang, H. J.; Yu, H.; Fang, Y. P. A Simple Preparation of Nitrogen Doped Titanium Dioxide Nanocrystals with Exposed (001) Facets with High Visible Light Activity. *Chem. Commun.* **2012**, *48*, 600−602.
(35) Shan, G. B.; Demopoulos, G. P. The Synthesis of Aqueous-Dispersible Anatase TiO_2 Nanoplatelets. *Nanotechnology* **2009**, *21*, 025604.
(36) Liu, G.; Yu, J. C.; Lu, G. Q.; Cheng, H. M. Crystal Facet Engineering of Semiconductor Photocatalysts: Motivations, Advances and Unique Properties. *Chem. Commun.* **2011**, *47*, 6763−6783.
(37) Kiatkittipong, K.; Scott, J.; Amal, R. Hydrothermally Synthesized Titanate Nanostructures: Impact of Heat Treatment on Particle Characteristics and Photocatalytic Properties. *ACS Appl. Mater. Interfaces* **2011**, *3*, 3988−3996.

DOI: 10.1021/acsami.5b00227
ACS Appl. Mater. Interfaces 2015, 7, 7995−8004

(38) Wu, M. M.; Lin, G.; Chen, D. H.; Wang, G. G.; He, D.; Feng, S. H.; Xu, R. R. Sol-Hydrothermal Synthesis and Hydrothermally Structural Evolution of Nanocrystal Titanim Dioxide. *Chem. Mater.* **2002**, *14*, 1974−1980.
(39) Zheng, Z. K.; Huang, B. B.; Lu, J. B.; Qin, X. Y.; Zhang, X. Y.; Dai, Y. Hierarchical TiO_2 Microspheres: Synergetic Effect of {001} and {101} Facets for Enhanced Photocatalytic Activity. *Chem.—Eur. J.* **2011**, *17*, 15032−15038.
(40) Wen, P. H.; Ishikawa, Y.; Itoh, H.; Feng, Q. Topotactic Transformation Reaction from Layered Titanate Nanosheets into Anatase Nanocrystals. *J. Phys. Chem. C* **2009**, *113*, 20275−20280.
(41) Du, Y.-E.; Feng, Q.; Chen, C. D.; Tanaka, Y.; Yang, X. J. Photocatalytic and Dye-Sensitized Solar Cell Perforemances of {010}-Faceted and [111]-Faceted Anatase TiO_2 Nanocrystals Synthesized from Tetratitanate Nanoribbons. *ACS Appl. Mater. Interfaces* **2014**, *6*, 16007−160019.
(42) Shi, X. C.; Zhang, Z. B.; Zhou, D. F.; Zhang, L. F.; Chen, B. Z.; Yu, L. L. Synthesis of Li^+ Adsorbent (H_2TiO_3) and Its Adsorption Properties. *Trans. Nonferrous Met. Soc. China* **2013**, *23*, 253−259.
(43) Tanaka, T.; Ebina, Y.; Takada, K.; Kurashima, K.; Sasaki, T. Oversized Titania Nanosheet Crystallites Derived from Flux-Grown Layered Titanate Single Crystals. *Chem. Mater.* **2003**, *15*, 3564−3568.
(44) Sarkar, D.; Ghosh, C. K.; Mukherjee, S.; Chattopadhyay, K. Three Dimensional Ag_2O/TiO_2 Type-II (p−n) Nanoheterojunctions for Superior Photocatalytic Activity. *ACS Appl. Mater. Interfaces* **2013**, *5*, 331−337.
(45) Zheng, J.-Y.; Bao, S.-H.; Guo, Y.; Jin, P. Anatase TiO_2 Films with Dominant {001} Facets Fabricated by Direct-Current Reactive Magnetron Sputtering at Room Temperature: Oxygen Defects and Enhanced Visible-Light Photocatalytic Behaviors. *ACS Appl. Mater. Interfaces* **2014**, *6*, 5940−5946.
(46) Tang, W. P.; Kanoh, H.; Yang, X. J.; Ooi, K. Preparation of Plate-Form Manganese Oxide by Selective Lithium Extraction from Monoclinic Li_2MnO_3 under Hydrothermal Conditions. *Chem. Mater.* **2000**, *12*, 3271−3279.
(47) Liu, Z.-H.; Ooi, K.; Kanoh, H.; Tang, W.-P.; Tomida, T. Swelling and Delamination Behaviors of Birnessite-Type Manganese Oxide by Intercalation of Tetraalkylammonium Ions. *Langmuir* **2000**, *16*, 4154−4164.
(48) Hou, W. H.; Chen, Y. S.; Guo, C. X.; Yan, Q. J. Synthesis of Porous Chromia-Pillared Tetratitanate. *J. Solid State Chem.* **1998**, *136*, 320−321.
(49) Tanaka, T.; Ebina, Y.; Takada, K.; Kurashim, K.; Sasaki, T. Oversized Titania Nanosheet Crystallites Derived from Flux-Grown Layered Titanate Single Crystal. *Chem. Mater.* **2003**, *15*, 3564−3568.
(50) Yang, X. J.; Makita, Y.; Liu, Z.-H.; Sakane, K.; Ooi, K. Structural Characterization of Self-Assembled MnO_2 Nanosheets from Birnessite Manganese Oxide Single Crystals. *Chem. Mater.* **2004**, *16*, 5581−5588.
(51) Chen, C. D.; Sewvandi, G. A.; Kusunose, T.; Tanaka, Y.; Nakanishi, S.; Feng, Q. Synthesis of {010}-Faceted Anatase TiO_2 Nanoparticles from Layered Titanate for Dye-Sensitized Solar Cells. *CrystEngComm* **2014**, *16*, 8885−8895.
(52) Howard, C. J.; Sabine, T. M.; Dickson, F. Structural and Thermal Parameters for Rutile and Anatase. *Acta Crystallogr., Sect. B* **1991**, *47*, 462−468.
(53) Liu, X. L.; Zhang, H. M.; Yao, X. D.; An, T. C.; Liu, P. R.; Wang, Y.; Peng, F.; Carroll, A. R.; Zhao, H. J. Visible Light Active Pure Rutile TiO_2 Photoanodes with 100% Exposed Pyramid-Shaped Surfaces. *Nano Res.* **2012**, *5*, 762−769.
(54) Momma, K.; Izumi, F. VESTA 3 for Three-Dimensional Visualization of Crystal, Volumetric and Morphology Data. *J. Appl. Crystallogr.* **2011**, *44*, 1272−1276.
(55) Feng, Q.; Hirasawa, M.; Yanagisawa, K. Synthesis of Crystal-Axis-Oriented $BaTiO_3$ and Anatase Platelike Particles by a Hydrothermal Soft Chemical Process. *Chem. Mater.* **2001**, *13*, 290−296.
(56) Chen, C. D.; Xu, L. F.; Sewvandi, G. A.; Kusunose, T.; Tanaka, Y.; Nakanishi, S.; Feng, Q. Microwave-Assisted Topochemical Conversion of Layered Titanate Nanosheets to {010}-Faceted Anatase Nanocrystals for High Performance Photocatalysts and Dye-Sensitized Solar Cells. *Cryst. Growth Des.* **2014**, *14*, 5801−5811.
(57) Zhang, T. Y.; Oyama, T.; Aoshima, A.; Hidaka, H.; Zhao, J. C.; Serpone, N. Photooxidative N-Demethylation of Methylene Blue in Aqueous TiO_2 Dispersions under UV Irradiation. *J. Photochem. Photobiol., A* **2001**, *140*, 163−172.
(58) Zhang, H. M.; Liu, P. R.; Li, F.; Liu, H. W.; Wang, Y.; Zhang, S. Q.; Guo, M. X.; Cheng, H. M.; Zhao, H. J. Facile Fabrication of Anatase TiO_2 Microspheres on Solid Substrates and Surface Crystal Facet Transformation From {001} and {100}. *Chem.—Eur. J.* **2011**, *17*, 5949−5957.
(59) Zhang, J.; Xu, Q.; Feng, Z. C.; Li, M. J.; Li, C. Importance of the Relationship between Surface Phases and Photocatalytic Activity of TiO_2. *Angew. Chem., Int. Ed.* **2008**, *47*, 1766−1769.
(60) Ohtani, B.; Kakimoto, M.; Nishimoto, S.; Kagiya, T. Photocatalytic Reaction of Neat Alcohols by Metal-Loaded Titanium-(IV) Oxide Particles. *J. Photochem. Photobiol. A Chem.* **1993**, *70*, 265−272.
(61) Yang, Y. C.; Wen, J. W.; Wei, J. H.; Xiong, R.; Shi, J.; Pan, C. X. Polypyrrole-Decorated Ag−TiO_2 Nanofibers Exhibiting Enhanced Photocatalytic Activity under Visible-Light Illumination. *ACS Appl. Mater. Interfaces* **2013**, *5*, 6201−6207.

DOI: 10.1021/acsami.5b00227
ACS Appl. Mater. Interfaces 2015, 7, 7995−8004